

Cavity-Quantum Electrodynamics with Moiré Flatband Photonic Crystals

Yu-Tong Wang,^{1,*} Qi-Hang Ye,^{2,*} Jun-Yong Yan,^{1,*} Yufei Qiao,^{2,1} Chen Chen,¹ Xiao-Tian Cheng,¹ Chen-Hui Li,¹ Zi-Jian Zhang,¹ Cheng-Nian Huang,¹ Yun Meng,^{3,4} Kai Zou,^{3,4} Wen-Kang Zhan,^{5,6} Chao Zhao,^{5,6} Xiaolong Hu,^{3,4} Clarence Augustine T H Tee,⁷ Wei E. I. Sha,¹ Zhixiang Huang,⁸ Huiyun Liu,⁹ Chao-Yuan Jin,^{1,10,†} Lei Ying,^{2,‡} and Feng Liu^{1,10,§}

¹State Key Laboratory of Extreme Photonics and Instrumentation,
College of Information Science and Electronic Engineering, Zhejiang University, Hangzhou 310027, China

²School of Physics, Zhejiang Key Laboratory of Micro-nano Quantum
Chips and Quantum Control, Zhejiang University, Hangzhou 310027, China

³School of Precision Instrument and Optoelectronic Engineering, Tianjin University, Tianjin 300072, China

⁴Key Laboratory of Optoelectronic Information Science and Technology, Ministry of Education, Tianjin 300072, China

⁵Laboratory of Solid State Optoelectronics Information Technology,
Institute of Semiconductors, Chinese Academy of Sciences, Beijing 100083, China

⁶College of Materials Science and Opto-Electronic Technology,
University of Chinese Academy of Science, Beijing 101804, China

⁷College of Physics and Electrical Information Engineering,
Zhejiang Normal University, Hangzhou 310058, China

⁸Key Laboratory of Intelligent Computing and Signal Processing,
Ministry of Education, Anhui University, Hefei 230039, China

⁹Department of Electronic and Electrical Engineering, University College London, London WC1E 7JE, UK

¹⁰International Joint Innovation Center, Zhejiang University, Haining 314400, China

(Dated: November 27, 2024)

Quantum emitters are a key component in photonic quantum technologies. Enhancing their single-photon emission by engineering the photonic environment using cavities can improve the overall efficiency in quantum information processing. However, this enhancement is often limited by the need for precise nanoscale control over emitter's position within micro/nano-cavities. Inspired by the fascinated physics of moiré pattern, we present an approach to strongly modify the spontaneous emission rate of a quantum emitter using fine-designed multilayer moiré photonic crystal with a robust isolate-flatband dispersion. Theoretical analysis reveals that due to its nearly infinite photonic density of states, the moiré cavity can simultaneously possess high Purcell factor and large tolerance over emitter's position. We experimentally demonstrate the coupling between this moiré cavity and a quantum dot via the cavity-determined polarization of the dot's emission. The radiative lifetime of the quantum dot can be tuned by a factor of 40 from 42 ps to 1692 ps, attributed to strong Purcell enhancement and Purcell inhibition effects. Our findings pave the way for moiré flatband cavity-enhanced quantum light sources, quantum optical switches and quantum nodes for quantum internet.

Introduction

Controlling individual single photons, i.e. the fundamental units of light described by Fock or number states [1], generated from a quantum emitter [2–4] is one of the major challenges in wide range from quantum optics [5] to quantum information technologies [6]. An efficient approach to manipulating single-photon emission rate and wave packets is by artificially modifying photonic environments surrounding quantum emitters, since the emission properties are dictated by these photonic modes. Given their ability to reshape the spatial and frequency distribution of electromagnetic waves, optical cavities stand out as the most powerful and versatile tool for coherent single-photon control, forming the field of cavity-quantum electrodynamics (cavity-QED) [7].

Traditionally made of general mirrors, cavities confine light waves at various scales. At macro-scale Fabry-Pérot cavities use traditional mirrors to trap light, while at mesoscopic scale cavities in nanophotonics use defects in photonic crys-

tals (PhCs) or distributed Bragg reflectors (DBRs) for realizing similar confinement. In the latter case, traditional mirrors are replaced with effective optical “walls” like the PhCs with a frequency bandgap or DBRs, in both of which electromagnetic field exponentially decay beyond the cavity boundary. These approaches have found success in various areas. In recent years, cavity-QED has delved into the intricate interplay between quantum emitters and fine-designed optical cavities, revealing a range of phenomena such as the Purcell effect in the weak coupling regime [8–10], strong coupling [11–13], and dipole-induced transparency [14–16]. In addition, more exotic cavities with specialized functions are proposed to enhance the photon emission such as photonic hyperbolic metamaterials [17] and surface plasmon in metallic structures [18], or to slow down the photon emission utilizing photonic structures with unique photonic dispersion relationships such as the specific PhCs with Dirac [19] or Weyl [20, 21] dispersion relationships and near-zero index materials [22]. In general, the Purcell effect predicts that, overall, the photon emission rate of a system is inversely proportional to the mode volume while directly proportional to the Q factor [23]. This implies that to sustain a high spontaneous emission rate from a quantum emitter, a small mode volume and a large Q factor are essential. While a large Q factor is often constrained by fabrication

* These authors contributed equally

† Email to: jincy@zju.edu.cn

‡ Email to: leiyang@zju.edu.cn

§ Email to: feng.liu@zju.edu.cn

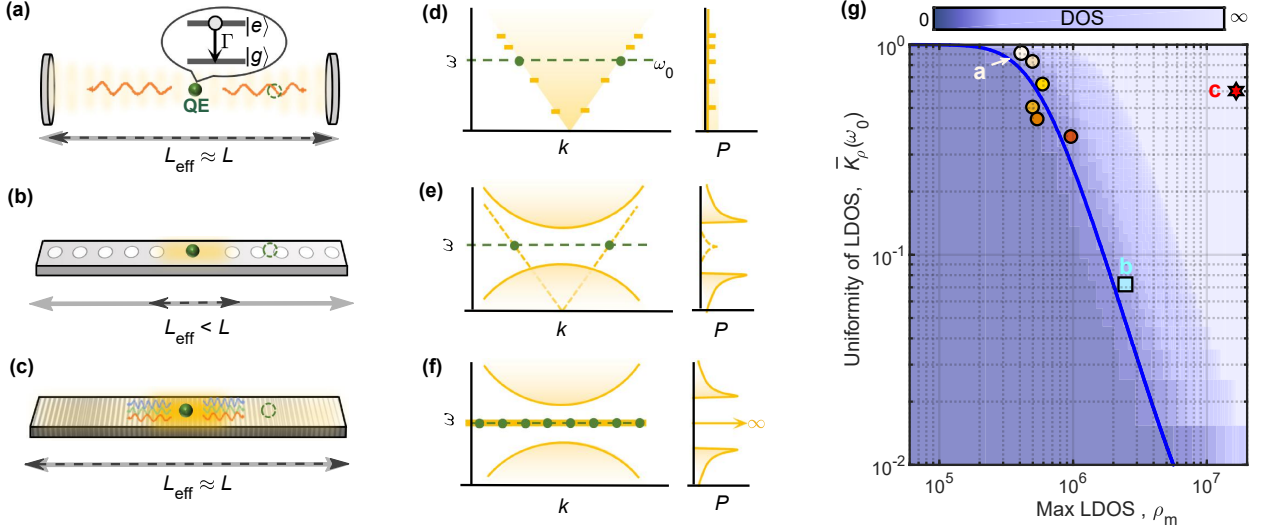


Figure 1. **Schematics of photon emission in various photonic structures.** A quantum emitter marked by green filled circle, respectively placed in (a) a traditional Fabry-Pérot cavity, (b) 1D defect PhC cavity, and (c) moiré PhC cavity. Green dashed circles stand for quantum emitters positioned at non-optimal sites. Black dashed double arrows stand for the effective length of cavities with strong LDOS, while the grey double arrows denote the full lengths of photonic structures. A quantum emitter is a quantum system with two energy levels: a ground state and an excited state, as illustrated in the inset of (a). When the quantum system transitions from the excited state to the ground state, it emits a single photon with a spontaneous emission rate Γ . Left and right panels of (d-f) represent the dispersion relations and DOS $P(\omega)$ of photonic structures in (a-c), respectively. Green dots denote the effective modes in (a-c) and green dashed lines mark the transition frequency of the quantum emitter ω_0 . Dashed yellow curves in (e) denote the dispersion or DOS inside the defect PhC cavity, distinguishing from those in bandgap PhC regime marked by solid yellow curves. (g) Schematically shows the uniformity of LDOS ($\bar{K}_p = 3 - \text{Kurt}\rho(\omega_0, x)$) versus the maximum value of LDOS ($\rho_m(\omega_0)$) for different fixed DOSs. Circles and squares stand for the numerical results of the (L3, L5, L7, L10, L15, L20) and H1 defect PhC cavities, respectively, from top to bottom. Here, we use the L20 cavity as an analogy to the traditional Fabry-Pérot cavity in (a). Red star represents the moiré PhC cavity. See numerical details in Supplementary Section III.

imperfections and the fundamental diffraction limit for many cavity designs [24], a small mode volume presents additional challenges related to extremely precise emitter positioning to maximize its exposure to the local field [25].

Inspired by the fascinated physics of moiré superlattices in electronic and excitonic systems [26–28], its photonic counterpart [29–33] offers the potential for confining photons due to its isolated flatband dispersion relation. This theoretically leads to an infinite photonic density of states at a fixed frequency, enabling simultaneous realization of an infinite Q factor and a large tolerance of emitter’s location within the cavity.

In this work, we propose utilizing the moiré flatband photonics to modify the Purcell effect and experimentally manipulate single photon emission from a semiconductor quantum dot (QD) within a robust quasi-1D triple-layer moiré cavity, eliminating the need for conventional mirrors and boundaries. Theoretical analysis shows that, due to its nearly infinite photonic density of states (DOS), both high Purcell factor and large tolerance over emitter position can be obtained simultaneously. The formation of the flat photonic band and resulting light localization are confirmed by the photoluminescence (PL) spectra and mapping. A large tuning range (from 42 ± 1 to 1692 ± 7 ps) of the QD’s radiative lifetime is achieved while scanning the detuning between the QD and the moiré cavity, with an experimentally realized Q factor of 3523. The QD and moiré PhC fabricated from III-V semicon-

ductor is grown directly on silicon. Our work demonstrates cavity-QED with moiré PhC, opening the door towards moiré flatband cavity-enhanced quantum optical devices compatible with silicon photonic platform [34–37].

Quantum emitter in flatband photonics

Here, we focus on quasi-1D systems as shown in Figs. 1(a-c). We suppose the photon volume as $V \approx AL$, where A is the average cross-sectional area of quasi-1D structure and L is the length of the photonic structure or the period of PhC. Spatial confinement of a single photon by generic “mirrors” is radically determined by the photonic DOS $P(\omega)$ of the photonic structure as the spontaneous emission rate of a quantum emitter Γ is proportional to the local density of states (LDOS). The photonic DOS and LDOS of a quasi-1D structure are respectively given by (see details in Supplementary Section II)

$$P(\omega) = \int_0^L \rho(\omega, x) dx, \quad (1)$$

and

$$\rho(\omega_0, x) \approx \frac{\hbar}{4\pi A} \sum_n \int_{\{k:\omega_k=\omega_0\}} \frac{|\epsilon_{n,k}(x)|^2}{v_g(k)} dk, \quad (2)$$

where $v_g(k)$ is the group velocity and $\epsilon_{n,k}(x)$ is the electric field density of the eigenmode (n, k) . Here, k denotes the momen-

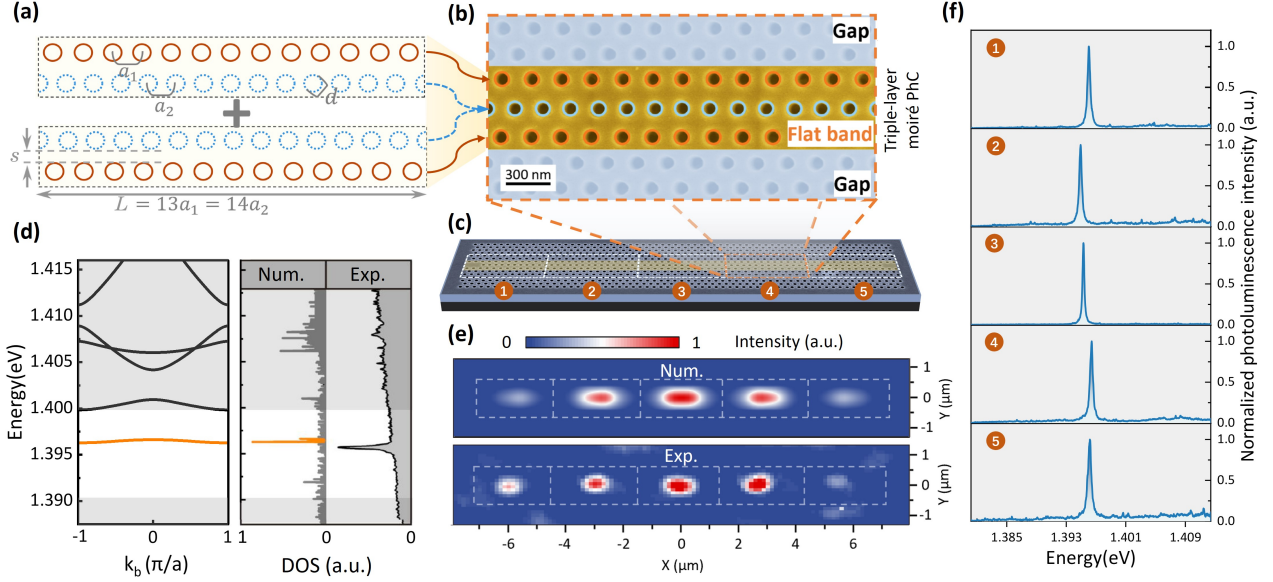


Figure 2. **Design and characterization of moiré flatband cavity.** (a) Two unit cells (gray dashed rectangles) of 1D moiré PhC composed of two 1D PhCs (brown and blue circles) with slightly different lattice constants ($a_1 = 209.1$ nm, $a_2 = 194.1$ nm). Other structural parameters: $d = 133$ nm, $s = 95$ nm, $L = 2718$ nm. (b) SEM image of a fabricated triple-layer moiré PhC unit cell formed by combining two unit cells shown in (a). (c) SEM image of a moiré PhC consisting of 5 unit cells (white dashed rectangles). (d) Right: Comparison of calculated and experimentally measured photon density of states. The latter is obtained by spatially integrating PL spectra within a moiré PhC unit cell. Orange color indicates the flatband mode. (e) Field spatial distribution of moiré flatband modes. Upper: Numerical calculation accounting for the spatial resolution of the subsequent optical measurement. Lower: PL map acquired by scanning the excitation and collection spots over the moiré PhC and recording the maximal PL intensity within $1.3939 - 1.3978$ eV. The FWHM of the excitation/collection spot is ~ 1.5 μm . (f) PL spectra of moiré cavity mode measured at centers of 5 moiré PhC unit cells marked in (c) under high-power above-barrier excitation. All experiments in this study are performed at $T = 3.6$ K. The Q factor of moiré cavity modes (1)-(5) are 3309, 3412, 5026, 3134 and 2602, respectively.

tum, n represents the photonic band index in a PhC, and x represents the location of the quantum emitter. In general, the uniformity of LDOS over the spatial dimensions and the maximum LDOS are two important properties. The latter one is denoted by ρ_m . The former one, depicted by the uniformity $\bar{K}_\rho \equiv 3 - \text{Kurt}\rho(\omega_0, x)$, indicates the tolerance for quantum emitter placement in a photonic structure exhibiting a strong spontaneous emission rate. Here, $\text{Kurt}(\cdot)$ represents the normalized kurtosis function.

Based on the relationship in Eqs. (1) and (2), we find that for a fixed LDOS at the quantum emitter's transition frequency ω_0 , there exists a trade-off between the spatial uniformity of the LDOS and the maximum LDOS ρ_m within a general quasi-1D photonic structure, as illustrated by the contour diagram in Fig. 1(g). This agrees with the empirical conclusion that a defect PhC cavity with a small effective mode volume (AL_{eff}) has a stronger enhancement of the spontaneous emission rate for a quantum emitter (or LDOS). For instance, the defect PhC cavities in Figs. 1(b,e) exhibit a finite LDOS at the resonant frequency ω_0 . The local field can be moderately enhanced by decreasing the number of filling holes from multi holes (L20-L3) to one hole (H1). This enhancement is accompanied by a decrease in the effective photon volume and results in a reduced \bar{K}_ρ . The theoretical prediction can be confirmed by our numerical simulations, as shown in Fig. 1(g).

A similar trend can be observed in Fabry-Pérot cavities (see Fig. 1(a,d)).

Now, we investigate an idealized scenario: a PhC structure with an isolated flatband dispersion relation, as shown in Figs. 1(c,f). This configuration yields a divergent DOS in the frequency domain and the localization in real space [38], as illustrated in Figs. 1(f) and (c) respectively. This implies that the spontaneous emission rate can reach an exceptionally high value when the quantum emitter is placed in suitable locations, while the uniformity of LDOS can be maintained at a reasonable level. Then, we numerically confirm an optimally designed moiré PhC structure described in the following text. As shown in Fig. 1(g), this structure can exhibit a ρ_m that is nearly two orders of magnitude higher than that of the L20 cavity, while maintaining a same level of \bar{K}_ρ to the L20 cavity (see in Supplementary Section III).

Here, we emphasize that if the quantum emitter is located in a non-optimal regime, i.e. its LDOS $\rho(x_0)$ is not at the maximum LDOS position (as illustrated by the dashed circles in Fig. 1(a-c)), the behavior changes. For a FP cavity, the spontaneous emission rate is slightly modified by changing the quantum emitter's position. In the case of a defect cavity, if the quantum emitter is placed out of the defect, the emission is significantly suppressed. However, for an ideal isolated flatband, the emission rate of a quantum emitter can be large at

most locations due to its infinite DOS at a fixed frequency ω_0 . On the other hand, in the frequency domain the flatband PhC exhibits maximum DOS, enabling it to function as a quantum emitter switch controlling both ultra-fast and ultra-slow photon emission.

Moiré flatband cavity

To study the single photon emission of a QD embedded in a flatband moiré PhC, firstly we design and fabricate a quasi-1D moiré PhC structure. This is composed of two types of 1D PhCs depicted by two lines of blue and brown circles in Fig. 2(a). The lattice constants (a_1 and a_2) of the two 1D PhCs satisfy the condition $L = 13a_1 = 14a_2$, which is a key requirement for the formation of a moiré PhC. The separation between two 1D PhCs, referred to as the magic distance (s), determines the flatness and frequency of the resulting moiré flatband. This moiré PhC confines light waves along the axis of the 1D PhC. We further introduce a triple-layer moiré PhC design (see Fig. 2(b)) by combing the two aforementioned structures. Such a multilayer moiré PhC is more robust to lattice constant variations, preserving a higher Q factor (see Fig. S6) [39]. Additionally, to achieve in-plane 2D confinement, we expand 1D PhCs on both upper and lower sides (shaded areas in Fig. 2(b)), providing light confinement in the longitudinal direction. Numerical simulations indicate a quality factor $Q = 4.65 \times 10^5$ (see details in Supplementary Note III). Fig. 2(c) shows the scanning electron microscopy (SEM) image of the moiré PhC consisting of 5 unit cells (labelled ‘1’ to ‘5’) fabricated within a suspended gallium arsenide (GaAs) membrane containing indium gallium arsenide (InGaAs) QDs.

It is worth noting that the entire device, including the QD and moiré PhC, is fabricated from III-V semiconductor grown directly on a silicon substrate using the molecular beam epitaxy technique (see details in Supplementary Fig. S2(b)). This heterogeneous integration approach is technically demanding due to the difficulty of growing high-quality crystals on a lattice-mismatched substrate. However, it is a key step towards large-scale integrated quantum photonic circuits based on mature silicon photonic platform [34–37], which are currently limited by the absence of high-performance deterministic quantum light sources due to the indirect bandgap of silicon.

To verify the dispersion relation of the designed moiré PhC, we perform the full-wave simulation, yielding a nearly flatband across the entire momentum space (see the orange curve in the left panel of Fig. 2(d)). The existence of such a nearly flatband is further confirmed by the consistence of the calculated photonic DOS as shown in Fig. 2(d) (Num.) and the peak of the spatially integrated PL spectrum of a moiré PhC unit cell measured under high excitation laser power (see Fig. 2(d) (Exp.)). All measurements in this work were conducted at $T = 3.6$ K.

One of the most interesting consequences of the flatband is the localization of light. This phenomenon is demonstrated and cross-checked by the spatial field distribution and PL spectra. The calculated field distribution shows that each unit cell of the moiré PhC acts as a cavity. The light field is well confined within five unit cells (see Fig. 2(e) (Num.)). This

simulation accounting for the spatial resolution (1.5 μm) of our optical measurement agrees well with the PL map measured by scanning the overlapping excitation and collection spots across the fabricated moiré PhC (see Fig. 2(e) (Exp.)). In addition, the spectrally resolved PL signal acquired at the center of each moiré PhC unit cell exhibits a distinct peak with a maximum Q factor of 5026 at the energy of around 1.396 eV (see Fig. 2(f)). Again, this confirms the light localization in the moiré PhC. The minor variations in resonant frequencies of moiré cavities are attributed to slight differences in lattice constants of each PhC unit cell caused by nanofabrication imperfections. The sufficient uniformity of moiré cavity modes demonstrates their high potential for constructing scalable arrays of identical cavity-enhanced quantum light sources.

Control of single photon emission

Following the characterization of the moiré PhC, we proceed to manipulate the spontaneous emission of a quantum emitter using the moiré flatband cavity. The first step is to identify a QD coupled with a moiré cavity. Fig. 3(a) shows magneto-PL spectra of a QD located in a moiré cavity. The position of the QD is indicated by the red trapezoid in the insert. This result is measured under low excitation laser power with a cryogenic confocal microscope. The presence of both the QD emission (indicated by red dashed lines) and the moiré cavity mode (indicated by the green dotted line) in the same spectra confirms the spatial overlap between them. The single-photon nature of the QD emission is verified in a standard Hanbury Brown and Twiss (HBT) setup [40]. Figure 3(b) presents a typical result showing strong antibunching and a single-photon purity of 0.93 ± 0.09 without any background subtraction, which unambiguously proves the PL signal originates from a quantum emitter.

Moreover, the coupling between the QD and moiré cavity can be proved by the polarization measurement. Typically, due to the Zeeman effect, the emission of a In(Ga)As QD subjected to a strong magnetic field in Faraday geometry splits into two branches with opposite circular polarizations [41]. In contrast, modified by the moiré cavity, here the photon emission from the upper branch in Fig. 3(a) exhibits predominantly linear polarization. In particular, its polarization measured at a high magnetic field of $B = 6$ T aligns well with that of the cavity mode, as shown in Fig. 3(c). Therefore, this observation can be attributed to the QD-moiré cavity coupling, where the cavity mode dictates the polarization of the QD emission.

Finally, we demonstrate the control over spontaneous emission of a quantum emitter by the moiré cavity. Fig. 3(d) shows the time-resolved PL (TRPL) of the QD measured at different QD-cavity detunings using a superconducting nanowire single photon detector (SNSPD) [42]. At $B = 7$ T where the QD and cavity are on resonance (see Fig. 3(a)), the TRPL (yellow dots in Fig. 3(d)) measured under longitudinal acoustic (LA) phonon-assisted excitation [43, 44] yields a radiative lifetime T_1 as short as 42 ± 1 ps (50 ± 1 ps) with (without) deconvolving the instrument response function (FWHM = 71 ± 1 ps). This lifetime corresponds to a 27 (22)-fold emission rate enhancement compared with the average lifetime $T_1' = 1121 \pm 3$ ps (green dots) for QD ensembles in GaAs bulk measured un-

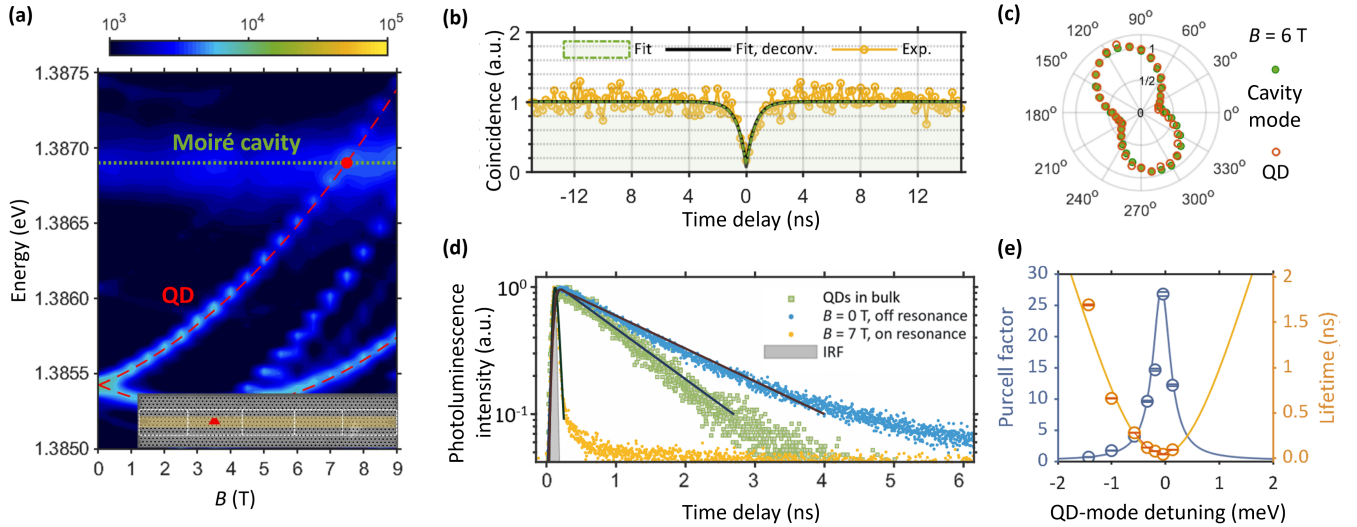


Figure 3. Manipulation of single photon emission from a QD in moiré flatband cavity. (a) Magnetic-field-dependent PL spectra of a QD and moiré cavity mode. The QD emission is split into two branches in external magnetic field applied parallel to the QD growth axis (Faraday geometry). The higher-energy branch is tuned to be resonant with the moiré cavity mode at $B = 7$ T. The red dot in the inset indicates the location of the QD in the moiré PhC. (b) Second-order correlation measurement of single photon emission from the QD under p-shell excitation. The black curve is obtained after deconvolving the detection response function from the green fit, yielding a single-photon purity of 0.93 ± 0.09 . The uncertainties correspond to one standard deviation from the fit. (c) Polarization of the emission from the QD (green) and moiré cavity mode (red) characterized at $B = 6$ T. The PL intensity is measured as a function of the half-wave plate angle in front of a linear polarizer. (d) Time-resolved PL of the QD measured using an SNSPD. Gray: instrument response function (IRF) with a FWHM of 71 ± 1 ps. Blue (orange): single QD detuned (resonant) with moiré cavity mode under LA phonon-assisted excitation. Green: QD ensemble in bulk under above-bandgap excitation. Black curves: single exponential fit. (e) QD-cavity detuning dependence of Purcell factor and QD lifetime. Solid lines: Lorentzian fit with a fixed FWHM. Error bars represent the uncertainty extracted from exponential fitting.

der above-barrier excitation. While at $B = 0$ T with the QD far detuned from the moiré cavity mode, T_1 slows down to 1692 ± 7 ps (blue dots in Fig. 3(b)) due to the Purcell inhibition [45–48].

Figure 3(e) summarizes the dependence of T_1 and the Purcell factor ($F_p = T_1'/T_1$) on the QD-cavity detuning. The experimental data can be well fitted using the model describing Purcell effect [49] with the measured cavity linewidth (0.394 meV). As shown in Fig. 3(e), T_1 varies by more than one order of magnitude over a detuning range 1.427 meV, demonstrating the effective control over QD's spontaneous emission by the moiré cavity.

Discussion and outlook

In summary, we have investigated cavity-QED with a moiré flatband PhC containing a quantum emitter. The flatband formation in moiré PhC can be understood as a result of the interference of multiple optical modes [50–52]. Compared to conventional cavities, e.g. Fabry–Pérot cavity and PhC defect cavities [23], one of the key advantages of moiré flatband PhC is the extremely high photonic LDOS. This enables efficient control over the QD's emission properties, including the polarization and radiative lifetime, as confirmed by the cavity-dominated polarization and a 40-fold tuning in radiative lifetime. This large tuning range is attributed to the pronounced Purcell enhancement and Purcell inhibition effects [45, 47].

Photonic bound states in the continuum (BIC) were also proposed with ultra-large DOS [53–55]. Compared with BIC, the flatband formed in the moiré PhC lies within a photonic bandgap, allowing the emission from a quantum emitter with finite linewidth being coupled into the flatband mode [54, 56]. By contrast, in the case of BIC, the portion of quantum emitter's emission that is not strictly resonant with the BIC mode can leak into radiative continuum modes, limiting the efficiency of Purcell enhancement.

As an outlook, combining the planar moiré PhC with various solid-state quantum emitters, including III-V QDs [57], color centers in diamond [58], 2D materials [59] and perovskite nanocrystals [60], could enable the development of arrays of cavity-enhanced on-chip quantum light sources [2, 49, 61–64], essential for large-scale quantum photonic circuits [34]. Further improving the Q factor may achieve strong coupling between quantum emitters and flatband photonic structure, with potential applications including quantum gates [65, 66], nondestructive photon detection [67], multiphoton graph states generation [68], ultrafast single-photon optical switch [69] and quantum nodes for quantum internet [70].

Acknowledgments

We acknowledge Prof. Alexander Tartakovskii for fruitful discussion. We acknowledge support from the National Key Research and Development Program of China (Nos. 2023YFB2806000, 2022YFA1204700, 2022YFA1404203), the National Natural Science Foundation of China (Nos. 62075194, 12375021, U21A6006, U20A20164), and the Engineering and Physical Sciences Research Council (EPSRC) of the United Kingdom (Nos. EP/P006973/1, EP/T028475/1, EP/X015300/1, EP/S030751/1, EP/V026496/1, EP/V006975/1).

Author contributions

F.L. and L.Y. conceived the project. Q.-H.Y. and C.-N.H. designed the moiré cavity, and performed simulations and theo-

retical derivations under the supervision of L.Y. and W.E.I.S. H.L., W.-K.Z., and C.Z. grew the wafer. Y.-T.W. and X.-T.C. fabricated the moiré cavity under the supervision of C.-H.L. and C.-Y.J. J.-Y.Y., C.C., Y.Q. and Z.-J.Z. carried out the quantum optics experiments under the supervision of F.L. Y.M. and K.Z. helped set up the SNSPD system under the supervision of X.H. J.-Y.Y., Y.-T.W., Q.-H.Y., L.Y., and F.L. analyzed the data. X.H., C.A.T. Tee, and Z.H. provided supervision and expertise. Y.-T.W., Q.-H.Y., J.-Y.Y., L.Y., and F.L. wrote the manuscript with comments and inputs from all the authors.

Competing interests

The authors declare no competing interests.

Data Availability

The data shown in the main text and supplementary materials are available from corresponding authors.

-
- [1] Scully, M. O. & Zubairy, M. S. *Quantum optics* (Cambridge university press, 1997).
- [2] Tomm, N. *et al.* A bright and fast source of coherent single photons. *Nature Nanotechnology* **16**, 399–403 (2021).
- [3] Dudin, Y. O. & Kuzmich, A. Strongly interacting rydberg excitations of a cold atomic gas. *Science* **336**, 887–889 (2012).
- [4] Kurtsiefer, C., Mayer, S., Zarda, P. & Weinfurter, H. Stable solid-state source of single photons. *Physical Review Letters* **85**, 290–293 (2000).
- [5] Walmsley, I. Quantum optics: Science and technology in a new light. *Science* **348**, 525–530 (2015).
- [6] Couteau, C. *et al.* Applications of single photons to quantum communication and computing. *Nature Reviews Physics* **5**, 326–338 (2023).
- [7] Walther, H., Varcoe, B. T., Englert, B.-G. & Becker, T. Cavity quantum electrodynamics. *Reports on Progress in Physics* **69**, 1325 (2006).
- [8] Arcari, M. *et al.* Near-unity coupling efficiency of a quantum emitter to a photonic crystal waveguide. *Physical Review Letters* **113**, 093603 (2014).
- [9] Lodahl, P., Mahmoodian, S. & Stobbe, S. Interfacing single photons and single quantum dots with photonic nanostructures. *Reviews of Modern Physics* **87**, 347–400 (2015).
- [10] Somaschi, N. *et al.* Near-optimal single-photon sources in the solid state. *Nature Photonics* **10**, 340–345 (2016).
- [11] Ohta, R. *et al.* Strong coupling between a photonic crystal nanobeam cavity and a single quantum dot. *Applied Physics Letters* **98**, 173104 (2011).
- [12] Reitzenstein, S. *et al.* Strong coupling in a single quantum dot semiconductor microcavity system. In Osinski, M., Henneberger, F. & Arakawa, Y. (eds.) *Proceedings of SPIE*, vol. 6115, 61151M (San Jose, CA, 2006).
- [13] Yoshie, T. *et al.* Vacuum rabi splitting with a single quantum dot in a photonic crystal nanocavity. *Nature* **432**, 200–203 (2004).
- [14] Javadi, A. *et al.* Single-photon non-linear optics with a quantum dot in a waveguide. *Nature Communications* **6**, 8655 (2015).
- [15] Söllner, I. *et al.* Deterministic photon–emitter coupling in chiral photonic circuits. *Nature Nanotechnology* **10**, 775–778 (2015).
- [16] Waks, E. & Vuckovic, J. Dipole induced transparency in drop-filter cavity-waveguide systems. *Physical Review Letters* **96**, 153601 (2006).
- [17] Cortes, C. L. & Jacob, Z. Super-coulombic atom–atom interactions in hyperbolic media. *Nature communications* **8**, 14144 (2017).
- [18] Gonzalez-Tudela, A. *et al.* Entanglement of two qubits mediated by one-dimensional plasmonic waveguides. *Phys. Rev. Lett.* **106**, 020501 (2011).
- [19] González-Tudela, A. & Cirac, J. I. Exotic quantum dynamics and purely long-range coherent interactions in dirac conelike baths. *Phys. Rev. A* **97**, 043831 (2018).
- [20] Ying, L. *et al.* Extended range of dipole-dipole interactions in periodically structured photonic media. *Phys. Rev. Lett.* **123**, 173901 (2019).
- [21] García-Elcano, I. n., González-Tudela, A. & Bravo-Abad, J. Tunable and robust long-range coherent interactions between quantum emitters mediated by weyl bound states. *Phys. Rev. Lett.* **125**, 163602 (2020).
- [22] Fleury, R. & Alù, A. Enhanced superradiance in epsilon-near-zero plasmonic channels. *Phys. Rev. B* **87**, 201101 (2013).
- [23] Tang, H., Ni, X., Du, F., Srikrishna, V. & Mazur, E. On-chip light trapping in bilayer moiré photonic crystal slabs. *Applied Physics Letters* **121**, 231702 (2022).
- [24] Vahala, K. J. Optical microcavities. *Nature* **424**, 839–846 (2003).
- [25] Badolato, A. *et al.* Deterministic coupling of single quantum dots to single nanocavity modes. *Science* **308**, 1158–1161 (2005).
- [26] Cao, Y. *et al.* Correlated insulator behaviour at half-filling in magic-angle graphene superlattices. *Nature* **556**, 80–84 (2018).
- [27] Mak, K. F. & Shan, J. Semiconductor moiré materials. *Nature Nanotechnology* **17**, 686–695 (2022).
- [28] Andrei, E. Y. *et al.* The marvels of moiré materials. *Nature Reviews Materials* **6**, 201–206 (2021).
- [29] Mao, X.-R., Shao, Z.-K., Luan, H.-Y., Wang, S.-L. & Ma, R.-M. Magic-angle lasers in nanostructured moiré superlattice. *Nature nanotechnology* **16**, 1099–1105 (2021).
- [30] Nguyen, D. X. *et al.* Magic configurations in moiré superlattice of bilayer photonic crystals: Almost-perfect flatbands and unconventional localization. *Phys. Rev. Res.* **4**, L032031 (2022).
- [31] Wang, X. *et al.* Experimental demonstration of high-efficiency harmonic generation in photonic moiré superlattice microcavities. *Nano Letters* **24**, 11327–11333 (2024).
- [32] Oudich, M., Kong, X., Zhang, T., Qiu, C. & Jing, Y. Engineered moiré photonic and phononic superlattices. *Nature Materials* **23**, 1169–1178 (2024).
- [33] Wang, P. *et al.* Localization and delocalization of light in pho-

- tonic moiré lattices. *Nature* **577**, 42–46 (2020).
- [34] Bao, J. *et al.* Very-large-scale integrated quantum graph photonics. *Nature Photonics* **17**, 573–581 (2023).
- [35] Arrazola, J. M. *et al.* Quantum circuits with many photons on a programmable nanophotonic chip. *Nature* **591**, 54–60 (2021).
- [36] Shang, C. *et al.* Electrically pumped quantum-dot lasers grown on 300 mm patterned si photonic wafers. *Light: Science & Applications* **11**, 299 (2022).
- [37] Wei, W.-Q. *et al.* Monolithic integration of embedded iii-v lasers on soi. *Light: Science & Applications* **12**, 84 (2023).
- [38] Di Benedetto, E., Gonzalez-Tudela, A. & Ciccarello, F. Dipole-dipole interactions mediated by a photonic flat band. *arXiv preprint arXiv:2405.20382* (2024).
- [39] Hao, C.-Y. *et al.* Robust flat bands in twisted trilayer graphene moiré quasicrystals. *Nature Communications* **15**, 8437 (2024).
- [40] Brown, R. H. & Twiss, R. Q. Correlation between photons in two coherent beams of light. *Nature* **177**, 27–29 (1956).
- [41] Bayer, M. *et al.* Fine structure of neutral and charged excitons in self-assembled in(ga)as/(al)gaas quantum dots. *Physical Review B* **65**, 195315 (2002).
- [42] Hao, Z. *et al.* High-performance eight-channel system with fractal superconducting nanowire single-photon detectors. *Chip* **3**, 100087 (2024).
- [43] Quilter, J. *et al.* Phonon-assisted population inversion of a single ingaas / gaas quantum dot by pulsed laser excitation. *Physical Review Letters* **114**, 137401 (2015).
- [44] Coste, N. *et al.* High-rate entanglement between a semiconductor spin and indistinguishable photons. *Nature Photonics* **17**, 582–587 (2023).
- [45] Bayer, M. *et al.* Inhibition and enhancement of the spontaneous emission of quantum dots in structured microresonators. *Physical Review Letters* **86**, 3168–3171 (2001).
- [46] Englund, D. *et al.* Controlling the spontaneous emission rate of single quantum dots in a two-dimensional photonic crystal. *Physical Review Letters* **95**, 013904 (2005).
- [47] Hulet, R. G., Hilfer, E. S. & Kleppner, D. Inhibited spontaneous emission by a rydberg atom. *Physical Review Letters* **55**, 2137–2140 (1985).
- [48] Lodahl, P. *et al.* Controlling the dynamics of spontaneous emission from quantum dots by photonic crystals. *Nature* **430**, 654–657 (2004).
- [49] Liu, F. *et al.* High purcell factor generation of indistinguishable on-chip single photons. *Nature Nanotechnology* **13**, 835–840 (2018).
- [50] Talukdar, T. H., Hardison, A. L. & Ryckman, J. D. Moiré effects in silicon photonic nanowires. *ACS Photonics* **9**, 1286–1294 (2022).
- [51] Nguyen, D. X. *et al.* Magic configurations in moiré superlattice of bilayer photonic crystal: Almost-perfect flatbands and unconventional localization. *Physical Review Research* **4**, L032031 (2022). ArXiv:2104.12774 [cond-mat, physics:physics].
- [52] Ma, R.-M. *et al.* Twisted lattice nanocavity with theoretical quality factor exceeding 200 billion. *Fundamental Research* **3**, 537–543 (2023).
- [53] Gao, X. *et al.* Formation mechanism of guided resonances and bound states in the continuum in photonic crystal slabs. *Scientific Reports* **6**, 31908 (2016).
- [54] Hsu, C. W., Zhen, B., Stone, A. D., Joannopoulos, J. D. & Soljačić, M. Bound states in the continuum. *Nature Reviews Materials* **1**, 16048 (2016).
- [55] Marinica, D. C., Borisov, A. G. & Shabanov, S. V. Bound states in the continuum in photonics. *Physical Review Letters* **100**, 183902 (2008).
- [56] Koshelev, K., Lepeshov, S., Liu, M., Bogdanov, A. & Kivshar, Y. Asymmetric metasurfaces with high-q resonances governed by bound states in the continuum. *Physical Review Letters* **121**, 193903 (2018).
- [57] Bayer, M. *et al.* Fine structure of neutral and charged excitons in self-assembled in(ga)as/(al)gaas quantum dots. *Physical Review B* **65**, 195315 (2002).
- [58] Sipahigil, A. *et al.* An integrated diamond nanophotonics platform for quantum-optical networks. *Science* **354**, 847–850 (2016).
- [59] He, Y.-M. *et al.* Single quantum emitters in monolayer semiconductors. *Nature Nanotechnology* **10**, 497–502 (2015).
- [60] Kaplan, A. E. *et al.* Hong–ou–mandel interference in colloidal cspbbr3 perovskite nanocrystals. *Nature Photonics* **17**, 775–780 (2023).
- [61] Michler, P. *et al.* A quantum dot single-photon turnstile device. *science* **290**, 2282–2285 (2000).
- [62] Ding, X. *et al.* High-efficiency single-photon source above the loss-tolerant threshold for efficient linear optical quantum computing. *arXiv* (2023). ArXiv:2311.08347 [quant-ph].
- [63] Liu, J. *et al.* A solid-state source of strongly entangled photon pairs with high brightness and indistinguishability. *Nature nanotechnology* **14**, 586–593 (2019).
- [64] Rota, M. B. *et al.* A source of entangled photons based on a cavity-enhanced and strain-tuned GaAs quantum dot. *eLight* **4**, 13 (2024).
- [65] Hacker, B., Welte, S., Rempe, G. & Ritter, S. A photon–photon quantum gate based on a single atom in an optical resonator. *Nature* **536**, 193–196 (2016).
- [66] Kim, H., Bose, R., Shen, T. C., Solomon, G. S. & Waks, E. A quantum logic gate between a solid-state quantum bit and a photon. *Nature Photonics* **7**, 373–377 (2013).
- [67] Niemietz, D., Farrera, P., Langenfeld, S. & Rempe, G. Non-destructive detection of photonic qubits. *Nature* **591**, 570–574 (2021).
- [68] Thomas, P., Ruscio, L., Morin, O. & Rempe, G. Efficient generation of entangled multiphoton graph states from a single atom. *Nature* **608**, 677–681 (2022).
- [69] Sun, S., Kim, H., Luo, Z., Solomon, G. S. & Waks, E. A single-photon switch and transistor enabled by a solid-state quantum memory. *Science* **361**, 57–60 (2018).
- [70] Kimble, H. J. The quantum internet. *Nature* **453**, 1023–1030 (2008).

METHODS

Wafer structure and sample fabrication

The sample is fabricated on an InGaAs QD wafer grown by molecular beam epitaxy (MBE) on a Si substrate. The wafer structure and detailed fabrication process are shown in Figure S1. The quantum dots are embedded at the center of a 140-nm GaAs membrane, with a sacrificial layer positioned underneath. After cleaning the wafer with acetone and isopropanol, an EBL resist (ARP-6200.13) is spin-coated onto the surface. The moiré pattern is then defined in the resist using electron beam lithography (Raith VOYAGER EBL system). Next, inductively coupled plasma etching (OXFORD Plasmapro 100 Cobra 180) is employed to transfer the pattern into the GaAs layer. Finally, wet etching is carried out to release the membrane, resulting in a suspended GaAs slab containing quantum dots.

Optical measurement

The schematic of the set-up for optical measurements is presented in Supplementary Fig. S1. The sample is located in a 3.6 K closed-loop cryostat (Attocube attoDRY), equipped with a magnetic field coil capable of generating up to $B = 9$ T of out-of-plane tunable magnetic field (Faraday geometry). For above-barrier excitation measurements, a 637 nm pump laser is used, produced by a continuous-wave (CW) diode laser (Thorlabs LP637). For p-shell excitation, the laser wavelength is set to 880 nm, generated by a tunable CW Ti:sapphire laser (M Squared Solstis). Emission signals are collected using a custom-built confocal microscope with a 0.85-N.A. objective lens. The collected photons are directed either to a spectrometer (Princeton Instruments HRS-750) with a 1800 grooves/mm grating for spectral analysis or to a superconducting nanowire single-photon detector for rapid single-photon detection. In TRPL measurements, the excitation pulse is provided by a tunable Ti:sapphire laser (Coherent Chameleon), emitting 150-fs pulses with an 80 MHz repetition rate. These pulses are then shaped to 8 ps using a home-made $4f$ pulse shaper. The pulses are tuned to the QD LA-phonon excitation sideband to minimize state preparation time jitter [43, 44]. The emitted single photons are filtered by double bandpass filters before being sent to the SNSPD. For field spatial distribution measurements, the excitation and the collection spots are precisely aligned (spot size $\sim 1.5 \mu\text{m}$). A two-dimensional raster scan with a step size of ~ 80 nm is performed using the xy-piezo nanopositioners (attocube ANPx101) below the sample.

Supplementary Materials

I. EXPERIMENTAL SETUP

The experimental setup used in this work is shown in Supplementary Fig. S1. Measurements were conducted using a confocal microscope with the sample placed in a closed-cycle cryostat and excited by either picosecond pulses or cw lasers. The QD emission was collected via a single-mode fiber and directed to one of three parts: a spectrometer for the measurement of PL spectra, a TRPL setup for lifetime measurements, or an HBT setup for single-photon purity analysis.

II. WAFER STRUCTURE AND SAMPLE FABRICATION PROCESS

Figure S2 (a) illustrates the wafer structure of the InGaAs quantum dot sample. A single layer of InGaAs QDs is at the center of a 140-nm GaAs membrane. To create a suspended membrane, a 1- μm $\text{Al}_{0.6}\text{Ga}_{0.4}\text{As}$ sacrificial layer is grown to make the GaAs membrane suspended. Below this structure, short-period PhC (SPL) and strained layer PhC (SLS) layers facilitate the transition between the Si substrate and the III-V semiconductor.

The process for fabricating the flatband structure, depicted in Fig. S2 (b), involves the following steps: First, the pattern is defined using electron beam lithography with the photoresist ARP-6200.13, followed by development in ARP600-546 for 1 minute. Subsequently, inductively coupled plasma etching is performed with a BCl_3/N_2 ratio of 2:3 to transfer the pattern into the GaAs layer, etching to a depth of 200 nm to ensure full penetration through the membrane. The sample is then immersed in a hydrofluoric acid solution (HF:DI = 1:5) for 15 minutes to remove the sacrificial layer beneath the pattern, resulting in a suspended GaAs slab featuring a moiré flatband structure.

III. THEORETICAL DERIVATION

A. Hamiltonians

We consider a quantum emitter (QE) embedding in PhC (PhC) structure. The QE can be modeled by a two-level system and its Hamiltonian is given by

$$\hat{H}_{\text{QE}} = \omega_0 \hat{\sigma}^\dagger \hat{\sigma}, \quad (\text{S1})$$

where ω_0 is the transition frequency of quantum dot and $\hat{\sigma}^\dagger$ ($\hat{\sigma}$) is the raising (lowering) operator. The Hamiltonian of PhC is written as

$$\hat{H}_{\text{PhC}} = \sum_{n,\mathbf{k}} \omega_{n,\mathbf{k}} \hat{a}_{n,\mathbf{k}}^\dagger \hat{a}_{n,\mathbf{k}}, \quad (\text{S2})$$

where $\omega_{n,\mathbf{k}}$ is the photon frequency for momentum n, \mathbf{k} . $\hat{a}_{n,\mathbf{k}}^\dagger$ ($\hat{a}_{n,\mathbf{k}}$) is the creation (annihilation) operator. The light-matter interaction term is

$$\hat{H}_{\text{int}} = \sum_{n,\mathbf{k}} \left[i g_{n,\mathbf{k}}(\mathbf{r}) (\hat{\sigma}^\dagger + \hat{\sigma}) \hat{a}_{n,\mathbf{k}}^\dagger e^{i n \cdot \mathbf{k} \cdot \mathbf{r}} + \text{h.c.} \right], \quad (\text{S3})$$

where $g_{n,\mathbf{k}}(\mathbf{r}) = \sqrt{\omega_{n,\mathbf{k}}/2\epsilon_0} \mathbf{V} \cdot \boldsymbol{\epsilon}_{n,\mathbf{k}}$ is the coupling between the photon labeled with n, \mathbf{k} and the QE at position \mathbf{r} . Here, $\boldsymbol{\mu}$ is the dipole matrix element of the QE and $\boldsymbol{\epsilon}_{\mathbf{k}}$ is the electric field of the mode \mathbf{k} .

B. Spontaneous emission rate and LDOS

The spontaneous emission rate can be derived from perturbation theory, where the interaction is considered as the perturbation, thus the transition matrix element is given by

$$M_{\text{FI}} = \langle F | \hat{H}_{\text{int}} | I \rangle + \sum_{\alpha} \frac{\langle F | \hat{H}_{\text{int}} | R_{\alpha} \rangle \langle R_{\alpha} | \hat{H}_{\text{int}} | I \rangle}{E_I - E_{R_{\alpha}}} + \dots \quad (\text{S4})$$

For small couplings, retaining terms up to the second term of expansion already achieves very high precision. The initial state and the final state are chosen to be the same, $|I\rangle = |F\rangle = |e; 0\rangle$. In the bracket 'e' means the quantum dot is at the excited state, the Arabic number indicate the number of photons in PhC. Two intermediate states are $|R_1\rangle = |g; 1_{n,\mathbf{k}}\rangle$ and $|R_2\rangle = |e; 1_{n,\mathbf{k}}\rangle$. The energy for state $|I\rangle$, $|R_1\rangle$ and $|R_2\rangle$ are respectively $E_I = E_e$, $E_{R_1} = \hbar\omega_{n,\mathbf{k}}$ and $E_{R_2} = E_e + E_e^{(n)} + \hbar\omega_{n,\mathbf{k}}$. In our discussion, The energy of $|g; 0\rangle$ serves as the zero-point of energy. The final result is given by [20]

$$M_{\text{FI}} = \sum_{n,\mathbf{k}} \left(g_{n,\mathbf{k}}(\mathbf{r}_m) g_{n,\mathbf{k}}^*(\mathbf{r}_n) \frac{1}{\omega_{n,\mathbf{k}} - \omega_0} + g_{n,\mathbf{k}}^*(\mathbf{r}_m) g_{n,\mathbf{k}}(\mathbf{r}_n) \frac{1}{\omega_{n,\mathbf{k}} + \omega_0} \right). \quad (\text{S5})$$

Replace the sum of \mathbf{k} by $V/(2\pi)^3 \int_{\text{1BZ}} d^3\mathbf{k}$ and take the imaginary part, we obtain the spontaneous emission rate as

$$\begin{aligned} \Gamma(\omega_0) &= \sum_n \int_{\text{1BZ}} d^3\mathbf{k} \frac{\omega_{n,\mathbf{k}}}{16\pi^2\epsilon_0} |\boldsymbol{\mu} \cdot \boldsymbol{\epsilon}_{\mathbf{k}}|^2 \delta(\omega_{n,\mathbf{k}} - \omega_0) \\ &= \sum_n \frac{\omega_0}{16\pi^2\epsilon_0} \int_{\{\mathbf{k}:\omega_{n,\mathbf{k}}=\omega_0\}} \frac{|\boldsymbol{\mu} \cdot \boldsymbol{\epsilon}_{\mathbf{k}}|^2}{|v_g(\mathbf{k})|} dS_{\mathbf{k}}. \end{aligned} \quad (\text{S6})$$

For the case of quasi-1D PhC structure, only k_x direction has continuous dispersion relation. Thus, the integral over iso-frequency surface reduced to the integral over the momentum direction k along x direction. Here, we use k represents the momentum along x direction. We assume that the electric field distribution at the $y-z$ cross section is uniform for each mode

k . The cross section area of the quasi-1D photonic structure is A . Then, the spontaneous emission can be re-written as

$$\Gamma(\omega_0) \approx \sum_n \frac{\omega_0}{4A\epsilon_0} \int_{\{k:\omega_k=\omega_0\}} \frac{|\boldsymbol{\mu} \cdot \boldsymbol{\epsilon}_{n,k}|^2}{v_g(k)} dk. \quad (\text{S7})$$

In general, the relationship between the spontaneous emission rate and photonic local density of state is given by

$$\Gamma(\boldsymbol{\mu} \rightarrow 1, \omega_0) = \sum_n \frac{\pi\omega_0}{\hbar\epsilon_0} \rho(\omega, \mathbf{r}), \quad (\text{S8})$$

the LDOS is given by

$$\rho(\omega, \mathbf{r}) = \sum_n \int_{\omega_k=\omega_0} \frac{\hbar}{16\pi^2 |v_g(\mathbf{k})|} |\boldsymbol{\epsilon}_{n,k}(\mathbf{r})|^2 dS_{\mathbf{k}}. \quad (\text{S9})$$

For quasi-1D scenario, we have

$$\rho(\omega_0, x) \approx \frac{\hbar}{4\pi A} \sum_n \int_{k \in \{\omega_k=\omega_0\}} \frac{|\boldsymbol{\epsilon}_{n,k}(x)|^2}{v_g(k)} dk. \quad (\text{S10})$$

C. Purcell factor

We use the general definition to derive the Purcell factor. At first, we consider the emission power

$$W = \frac{\omega}{2} \text{Im} [\boldsymbol{\mu} \cdot \mathbf{E}(\mathbf{r}_s)], \quad (\text{S11})$$

where $\boldsymbol{\mu}$ is the dipole element and \mathbf{r}_s is its position. The electric field is given by the Helmholtz equation:

$$\nabla \times \nabla \times \mathbf{E}(\mathbf{r}) - \epsilon(\mathbf{r})k_0^2 \mathbf{E}(\mathbf{r}) = i\mu_0 \omega \mathbf{j}(\mathbf{r}). \quad (\text{S12})$$

Alternatively, we can express the electric field with the Green's function

$$\mathbf{E}(\mathbf{r}) = i\mu_0 \omega \int \mathbf{G}(\mathbf{r}, \mathbf{r}', \omega) \mathbf{j}(\mathbf{r}') d\mathbf{r}', \quad (\text{S13})$$

where the Green's function can be obtained from

$$\nabla \times \nabla \times \mathbf{G}(\mathbf{r}, \mathbf{r}', \omega) - \epsilon(\mathbf{r})k_0^2 \mathbf{G}(\mathbf{r}, \mathbf{r}', \omega) = \mathbf{I}_{3 \times 3} \delta(\mathbf{r} - \mathbf{r}'). \quad (\text{S14})$$

For point-like quantum dipole, we have

$$W = \frac{\mu_0 \omega^3}{2} |\boldsymbol{\mu}|^2 \text{Im} [\hat{\boldsymbol{\mu}} \cdot \mathbf{G}(\mathbf{r}_s, \mathbf{r}'_s, \omega) \cdot \hat{\boldsymbol{\mu}}]. \quad (\text{S15})$$

In free space, the emission power is given by

$$W_0 = \frac{\omega^4}{12\pi\epsilon_0 c^3} |\boldsymbol{\mu}|^2. \quad (\text{S16})$$

Then, the Purcell factor is written as

$$F_P = \frac{W}{W_0} = \frac{6\pi}{k_0} \text{Im} [\hat{\boldsymbol{\mu}} \cdot \mathbf{G}(\mathbf{r}_s, \mathbf{r}'_s, \omega) \cdot \hat{\boldsymbol{\mu}}]. \quad (\text{S17})$$

With the eigenmodes $\mathbf{e}_n(\mathbf{r})$ of the Helmholtz equation, we can express the Green's function as

$$\mathbf{G}(\mathbf{r}, \mathbf{r}', \omega) = c^2 \sum_n \frac{\boldsymbol{\epsilon}_n(\mathbf{r}) \otimes \boldsymbol{\epsilon}_n^*(\mathbf{r}')}{\omega_n^2 - \omega^2 - i\omega\gamma_n}. \quad (\text{S18})$$

Here, the notation \otimes denotes the dyadic product. γ_n is the damping rate of mode n . For a periodic structure, to make the mode more explicit, we rewrite the Green's function as

$$\mathbf{G}(\mathbf{r}, \mathbf{r}', \omega) = \frac{Vc^2}{(2\pi)^3} \int \frac{\boldsymbol{\epsilon}_{n,\mathbf{k}}(\mathbf{r}) \otimes \boldsymbol{\epsilon}_{n,\mathbf{k}}^*(\mathbf{r}')}{\omega_{n,\mathbf{k}}^2 - \omega^2 - i\omega\gamma_{n,\mathbf{k}}} d^3\mathbf{k}, \quad (\text{S19})$$

where we use n labels the eigenenergy and \mathbf{k} labels the bloch vector in 1st Brillouin zone. As ω is close to a flatband, the summation in Eq. (S19) becomes extremely large and thus it will lead to strong Purcell enhancement.

IV. NUMERICAL RESULTS FOR DIFFERENT PHC CAVITIES

In Fig. S3, we present the distributions of the Purcell factor for the moiré structure, h1 cavity, and various L-type cavities. As shown, the moiré structure theoretically exhibits a significantly larger Purcell factor compared to conventional cavities, while still maintaining a considerable spatial extent. Theoretically, this feature breaks the conventional trade-off observed in traditional cavities, where the h1 and L3 cavities achieve relatively high Purcell factors but with small effective mode volume. Conversely, larger L-type cavities, such as L10, L15, and L20, offer a broader spatial extent while they have smaller Purcell factors. Same conclusions in LDOS distributions are shown in Fig. S4.

Figure S5(a) shows the bandgap area, which typically correlates with a high Q factor for the flatband within the bandgap. Figure S5(b) presents the numerical results for the Q factor of moiré cavity, showing a peak $Q \approx 1.6 \times 10^7$ at $d \approx 137.5$ nm, consistent with our expectations. This numerical results indicate that the bandwidth exhibits a significant reduction at $d \approx 137.5$ nm, implying a sharp flatness of the band. Therefore, we use $d = 137.5$ nm to realize the moiré flatband cavity.

Figure S6 presents the robustness analysis for the structure designed by us. Our design consists of three lines of holes with separations a_1 , a_2 , and a_1 , respectively, while the traditional two-line design consists of two lines of holes with separations a_1 and a_2 . As the difference in hole separations $\Delta a = a_1 - a_2$ changes by a small amount ($\pm 2.5\%$), our design shows a smaller and more linear change in the Q factor, while the traditional design exhibits a larger and non-linear change, indicating that the three-line design provides better robustness.

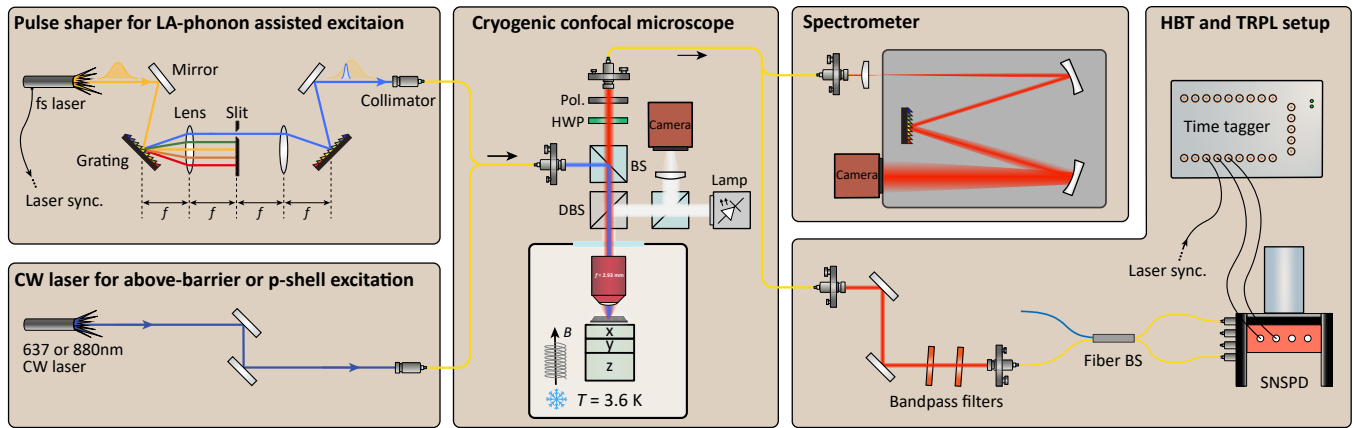


Figure S1. **Schematic of the setup for optical measurements.** Left panels: laser excitation part including $4f$ pulse shaping setup for LA-phonon-assisted excitation and CW lasers for above-barrier or p-shell excitation. Central panel: a home-built confocal microscope with the sample loaded in a closed-cycle cryostat ($T = 3.6$ K). Right panels: single-photon characterization part including spectrometer, HBT interferometer, and TRPL setup. Laser sync.: laser synchronization signal. Pol.: polarizer. HWP: half-wave plate. BS: beam splitter. DBS: dichroic beam splitter.

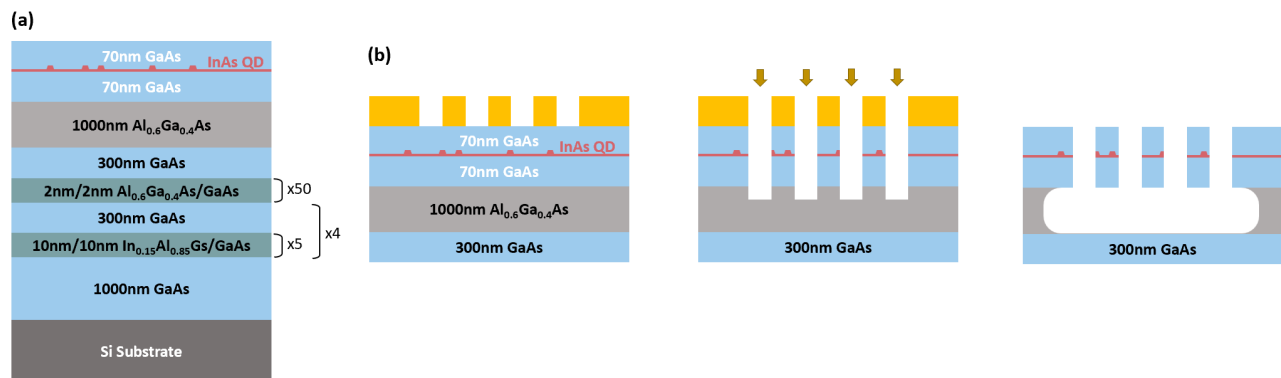


Figure S2. **Wafer structure and sample fabrication process.** (a) Wafer structure of the InGaAs quantum dot sample. (b) Process flow for patterning and etching to achieve a suspended GaAs slab.

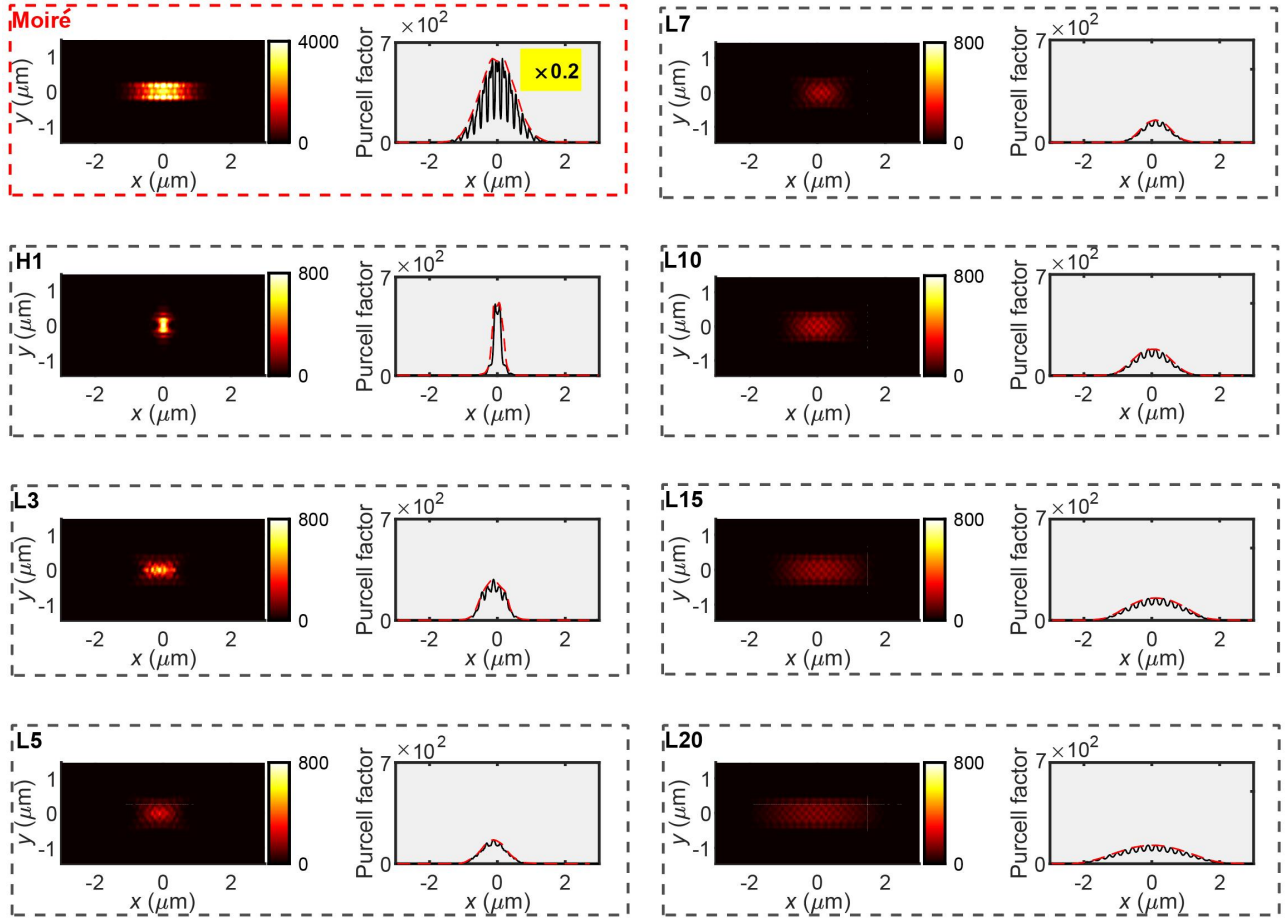


Figure S3. **Distribution of the Purcell factor for moiré lattice, comparing to conventional defect PhC cavities.** The left column presents the distribution in x-y plane. The right column is the corresponding result after averaging over the range $y = -400\text{nm}$ to 400nm , with the red dashed line representing the envelope of its distribution. For visualization purposes, the averaged Purcell factor for the moiré structure are scaled down by a factor of 5.

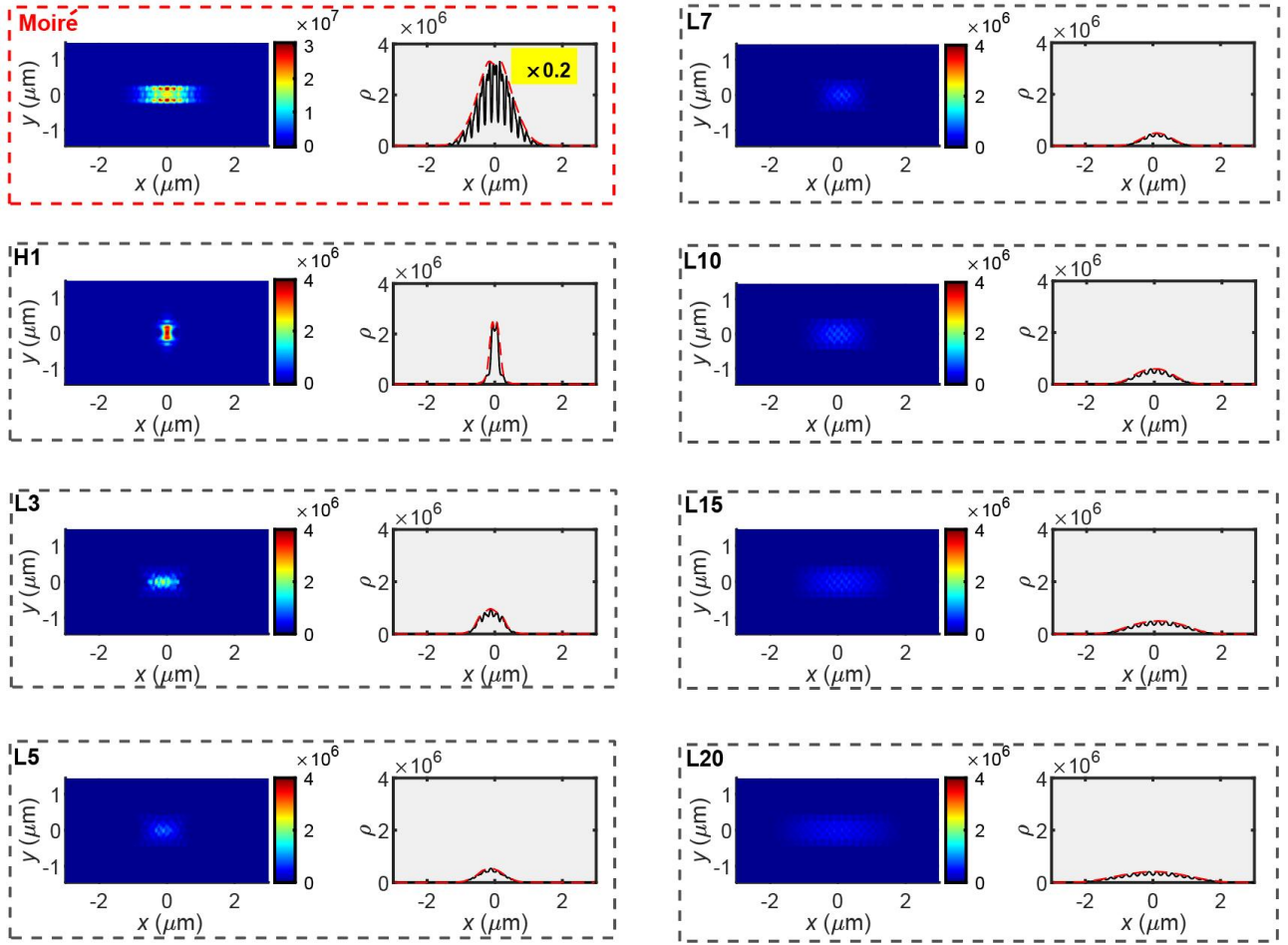


Figure S4. **Distribution of the LDOS for moiré lattice, comparing to conventional defect PhC cavities.** The left column presents the distribution in x-y plane. The right column is the corresponding result after averaging over the range $y = -400\text{nm}$ to 400nm , with the red dashed line representing the envelope of its distribution. For visualization purposes, the averaged LDOS values for the moiré structure are scaled down by a factor of 5.

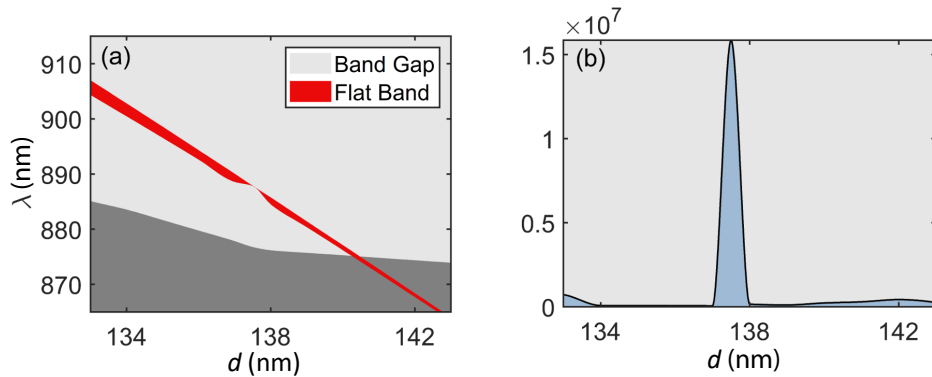


Figure S5. **Numerical results for varying hole diameter.** (a) Frequency shift of flatband as a function of hole diameter. The red band denotes the flatband mode and its width representing the bandwidth. The dark grey region represents the bulk modes while the light grey region stands for the bandgap. (b) Q factor as a function of hold diameter. A peak of $Q \approx 1.6 \times 10^7$ appears at around $d = 137.5\text{nm}$.

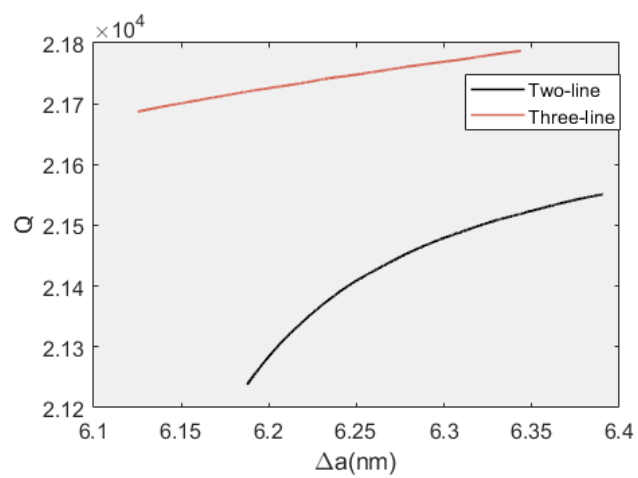


Figure S6. **Robustness test for two structures.** The Q factors of the two structures exhibit different sensitivities to perturbations in the lattice constant difference Δa .